International Journal of Transport Development and Integration
https://www.acadlore.com/journals/IJTDI

Design, Modeling, and Control of a Ćuk based DC-DC Converter for Hybrid Vehicle Applications

Hesham Al Salem[1], Abdulaziz Albuti[2], Saeed Alyami[2], Mohammad Obeidat[3*], Khaled Mahafzah[4], Ayman M. Mansour[5,6]

[1] Department of Mechanical Engineering, College of Engineering, Tafila Technical University, 66110 Tafila, Jordan
[2] Department of Electrical Engineering, Majmaah University, 91431 Al-Majmaah, Saudi Arabia
[3] Department of Electrical and Mechatronics Engineering, Tafila Technical University, 66110 Tafila, Jordan
[4] Department of Electrical Engineering, Al-Ahliyya Amman University, 19328 Amman, Jordan
[5] Department of Business Intelligence and Data Analysis, University of Petra, 1196 Amman, Jordan
[6] Department of Computer and Communications Engineering, Tafila Technical University, 66110 Tafila, Jordan

* Correspondence: Mohammad Obeidat (maobaidat76@ttu.edu.jo)

Received: 09-25-2025 **Revised:** 12-03-2025 **Accepted:** 12-15-2025

Citation: H. Al Salem, A. Albuti, S. Alyami, M. Obeidat, K. Mahafzah, and A. M. Mansour., "Design, modeling, and control of a Ćuk based DC-DC converter for hybrid vehicle applications," *Int. J. Transp. Dev. Integr.*, vol. 10, no. 1, pp. 76–92, 2026. https://doi.org/10.56578/ijtdi100106.

Abstract: DC-DC converters are vital in hybrid and electric vehicles, enabling efficient energy transfer and stable power management across batteries, auxiliary loads, and traction systems. Traditional Ćuk converters typically require high-voltage coupling capacitors, which increase size, cost, and reduce suitability for automotive use. This study presents a modified Ćuk-based DC-DC converter that reconfigures the conventional topology to utilize a lower-voltage coupling capacitor without changing the basic components. The design is analysed through state-space modelling, transfer function derivation, and integration of a control system to enhance dynamic response and stability. Simulation results obtained in MATLAB/Simulink under various duty cycles show significant improvements over the traditional Ćuk converter, including a 96.9% reduction in coupling capacitor voltage during steady-state operation and a 79.2% reduction in overshoot. These findings confirm the practicality, compactness, and efficiency of the proposed converter, making it a promising solution for reliable power management in hybrid and electric vehicles.

Keywords: DC-DC converter; State space; Hybrid vehicles; Average model; Ćuk converter

1 Introduction

DC-DC converters play a vital role in hybrid and electric vehicles, where efficient energy conversion and stable power flow are essential for reliable operation. Recent advances in power electronics have significantly improved the efficiency and performance of these converters, making them indispensable in automotive energy systems. Their ability to regulate and stabilize power transfer between energy storage devices such as batteries and super-capacitors and traction or auxiliary loads ensures consistent voltage and current levels under varying driving conditions. The integration of advanced control strategies further enhances their adaptability, enabling converters to maintain high efficiency across different load demands and environmental factors. This makes them particularly well-suited for hybrid vehicle powertrains, where energy sources and operating modes frequently change. The increasing demand for compact, efficient, and stable DC-DC converters underscores their importance as a core component in achieving reliable energy management and supporting the transition toward clean and sustainable transportation technologies. This paper focuses on investigating a newly proposed DC-DC Ćuk-type converter. It extends a previously published topology by developing a control system that enhances the converter's operational performance [1].

The Ćuk DC-DC converter can be effectively utilized in various automotive applications due to its unique advantages, including continuous input and output currents, low current and voltage ripple, and the capability to either step up or step down voltage with optional polarity inversion. These features make it particularly suitable for power conditioning in modern vehicles where efficiency, compactness, and electromagnetic compatibility are critical. One key application is in generating negative voltage rails required by automotive electronic subsystems

such as analog sensors, operational amplifiers, LiDAR front-end circuits, and display biasing units, where a stable and low-noise negative supply (e.g., -5 V or -12 V) is necessary. In electric and hybrid vehicles, the Ćuk converter can also serve as an intermediate power stage to step down or step up voltages between domains (e.g., from 48 V to 12 V) while minimizing electromagnetic interference (EMI), a vital aspect in high-voltage environments. Furthermore, it can be applied in LED lighting and display systems, functioning as a constant current source that ensures uniform illumination and reduced flicker across varying input voltages. In advanced driver assistance systems (ADAS), radar, and camera modules, the converter's low ripple characteristics help maintain stable and noise-free operation of sensitive analog and RF circuits. Additionally, in onboard charging systems of electric vehicles, modified Ćuk topologies can be employed to supply auxiliary low-voltage circuits from high-voltage buses without requiring isolation. Despite its benefits, implementing a Ćuk converter in automotive environments requires careful attention to design factors such as wide input voltage variation, load-dump transients, temperature robustness, and electromagnetic compatibility. Overall, the Ćuk converter represents a promising and efficient solution for specialized automotive power conversion applications that demand high stability, low ripple, and flexible voltage control [2].

The main contribution of this paper is the development and analysis of a modified Ćuk-based DC-DC converter that extends and improves the topology presented in study by Mahafzah et al. [1]. The proposed design substantially reduces the voltage stress across the coupling capacitor, enabling the use of a lower-voltage capacitor without altering the fundamental structure of the converter. A comprehensive nonlinear state-space model and full system transfer function are derived to allow accurate prediction of system behavior under varying duty-cycle conditions. An improved control strategy is also integrated to enhance transient response, minimize overshoot, and increase overall efficiency. Experimental validation, supported by close agreement with MATLAB/Simulink results, confirms the practical effectiveness of the proposed modifications, demonstrating a 96.9% reduction in steady-state coupling-capacitor voltage and a 79.2% reduction in overshoot compared to conventional designs. Collectively, these contributions—namely the modified converter topology, the complete analytical modeling framework, the enhanced control strategy, and the comprehensive experimental verification—establish the proposed converter as a compact, efficient, and practically viable solution for hybrid-vehicle power management. DC-DC converters are power electronic circuits designed to transform voltage levels, either within DC ranges or between DC and AC, depending on system requirements. Various approaches such as linear, switched-mode, capacitive, and magnetic methods are used to achieve this functionality [2]. These converters are generally classified according to their design principles, operational modes, voltage conversion characteristics, or structural configurations, which define the relationship between input and output. The following section outlines the main types of converters and their respective applications.

Typically, DC-DC converters operate within the medium-frequency range, with classification determined by circuit topology and function. They are especially important in applications that demand high efficiency or extended battery life, where linear regulators are unsuitable due to excessive power losses [3, 4]. Unlike linear systems, these converters employ capacitors and switches to regulate voltage and current efficiently, minimizing energy dissipation while ensuring stable operation.

To enhance efficiency, particularly in low-voltage applications, the diode in DC-DC converters can be replaced with a power MOSFET switch reducing voltage drop and improving power conversion as well as battery life [5]. In synchronous designs, two switches operate alternately to regulate output voltage under dynamic load conditions. These converters are attractive alternatives to linear regulators due to their low losses and high efficiency. However, they face limitations, such as dependence on PWM feedback, which requires a minimum output ripple for effective regulation, and sensitivity to duty cycle, making it difficult to achieve the ultra-low noise levels possible with linear regulators.

A boost converter, classified as a step-up converter, raises a lower input voltage to a stabilized higher output [6]. When the switch is closed, energy is stored in the inductor while the capacitor maintains load supply. Once the switch opens, the inductor releases energy, adding to the input, thereby increasing output voltage. The diode directs current to the load and recharges the capacitor [7].

Since the input current increases proportionally with the boost factor, a converter designed to triple the output voltage must also supply triple the input current. This rise in current can cause fluctuations and voltage drops, while requiring additional switches to turn off the output, which complicates the circuit design. Boost converters are therefore widely applied in solar power systems to optimize energy extraction and in power supply units [8].

When both step-up and step-down capability are required while maintaining the same input polarity, the non-inverting buck-boost converter is a suitable choice. In many applications, ensuring a stable voltage supply is crucial, as input levels may fluctuate above or below the required value [9, 10]. This topology integrates both buck and boost operations in a single circuit: the buck mode reduces voltage when input is higher, and the boost mode increases it when input is lower. The circuit typically includes an inductor, diode, switch, and capacitor, with the switch regulating energy transfer and output voltage. Unlike the conventional buck-boost converter, which inverts the output polarity, the non-inverting version maintains the same polarity, while providing continuous output current. This

makes it especially advantageous for systems requiring smooth and uninterrupted power delivery [11–13].

A major limitation of this type of converter is its circuit complexity, which increases design difficulty and overall cost. Additionally, switching regulators can generate EMI and noise that may affect nearby electronic components if not properly controlled. Non-inverting buck-boost converters are commonly used in automotive power systems and renewable energy applications, including solar energy [14–16]. The flyback converter represents an isolated variant of the traditional buck-boost converter, employing a transformer to electrically separate the input and output. The configuration introduces in study [16], explains how the regulated voltage is stored in the transformer core during the ON phase, and upon switching off, the energy is transferred to the secondary circuit, maintaining isolation between input and output.

The flyback converter differs from conventional converters mainly in its transfer function, which is influenced by the transformer turns ratio. Its key advantages include the ability to achieve high output voltage multiplication in short cycles, easy implementation of multiple outputs through additional secondary windings, and a low component count that reduces costs [17]. However, careful selection of the transformer core is essential to prevent saturation due to DC bias, and losses can occur due to magnetic hysteresis and eddy currents. Flyback converters are widely used in medical devices, isolated power supplies, telecom systems, and LED lighting [18, 19].

The Ćuk converter is a two-stage boost-buck topology that provides an inverted output voltage [20]. Unlike conventional buck-boost designs, it uses capacitors for energy transfer rather than solely relying on inductors. Its configuration includes at least two inductors, capacitors, a switch, and a diode, enabling continuous energy flow to the load. When the switch is closed, energy is stored in the inductors while capacitors supply the load, and after opening the switch, both inductors and capacitors continue to transfer energy, ensuring stable operation. A key advantage of this converter is its high efficiency, achieved through continuous current flow that minimizes energy losses, resulting in lower current ripple at both input and output compared to other converter. However, its main drawbacks include a more complex design and an inverted output voltage, which may limit its versatility for some applications. These converters are commonly used in automotive systems and noise-sensitive applications such as audio equipment or precision measurement devices [21–23].

The single-ended primary inductive converter (SEPIC) shares similarities with the Ćuk converter but addresses the inverted output limitation of traditional buck-boost designs. In SEPIC, the second inductor and diode are swapped, allowing the output voltage polarity to match the input, enhancing its applicability. The SEPIC converter maintains a constant output polarity, making it suitable for battery-powered applications such as rechargeable cells and battery chargers. Similar to the Ćuk converter, SEPIC exhibits a continuous input current waveform, which facilitates EMC filtering. It is commonly used in LED lighting systems, where the capacitor ensures short-circuit protection and the feedback loop can be adjusted to maintain a stable current flow. A key limitation of SEPIC is its pulsed waveform, akin to traditional buck-boost converters and unlike the Ćuk design. Its feedback system is complex, featuring a 4-pole function that can easily resonate.

The forward converter, comparable to the Flyback or half-bridge converter, provides output voltages that can be higher or lower than the input while ensuring electrical isolation via a transformer. Although more complex than the flyback converter, this configuration delivers higher output power and superior energy efficiency. The Flyback converter shares similarities with the buck converter, storing and delivering energy in a comparable manner. It uses a power MOSFET as the switching element, which alternates between open and closed states, similar to the forward converter [24]. Despite superficial similarities, the forward converter operates differently, offering several advantages. Notably, it achieves better transformer utilization by transferring energy directly through the transformer rather than relying on energy storage within it. This allows the use of transformers with higher magnetizing inductance and no air gap, reducing copper losses at lower peak currents. The primary output inductor stores most of the energy, enabling smaller capacitors and reducing output voltage ripple. Additionally, the forward converter experiences lower peak currents in active devices due to the larger magnetizing inductance. However, forward converters are more costly than Flyback designs because of the need for an output inductor and freewheeling diode, and they impose higher minimum load requirements, particularly in multi-output or high-voltage systems [25].

The push-pull converter is well-suited for medium- to high-power applications, offering higher efficiency and lower EMI compared to other converter types. It uses two switches operating in a push-pull configuration, typically with transistors, to convert DC input voltage into a higher or lower output voltage as required. In a push-pull converter, one switch conducts during the first half of the cycle while the other switch operates during the second half, creating alternating current in the primary windings of the transformer. The transformer adjusts the voltage up or down according to the turns ratio. It also provides electrical isolation between the input and output. The AC voltage from the secondary winding is rectified to DC using diodes, and capacitors and inductors are often employed as filters to smooth the output, ensuring a stable DC voltage. The system's key advantages include high efficiency over a wide range of voltages and loads, as well as excellent input-output isolation provided by the transformer. However, the push-pull converter is relatively complex due to multiple transistors and the transformer, resulting in higher costs. Additionally, it can produce significant electromagnetic interference if not properly shielded [26, 27].

The full-bridge converter is commonly employed in high-power applications due to its ability to efficiently manage large amounts of energy. It utilizes four power MOSFETs as switches arranged in an H-bridge configuration. The switches operate in diagonally opposite pairs, alternating the current direction through the transformer or inductors, thereby converting the DC input into an AC waveform [28]. Energy is transferred from the primary to the secondary side via a transformer or inductor, and the AC voltage is rectified and filtered to provide a stable DC output. Compared to other topologies, the Full-Bridge experiences lower voltage stress, contributing to its effectiveness [29]. This converter typically achieves efficiencies above 90% and can handle high input voltages and output currents. The inclusion of a transformer ensures galvanic isolation between stages, enhancing safety and preventing ground loop issues [30].

2 Modelling and Analysis of a New Ćuk-Based DC-DC Converter

In Figure 1 below, the arrangement of some elements is different in the new Ćuk converter, but contains almost all the elements found in the traditional Ćuk converter. The only switch for this converter is M_1, a power MOSFET transistor, able to handle high power with very short switching times. In energy storage, it has two inductors, L_1 and L_2, and two energy storage capacitors, C_1 and C_0. The converter also has a rectifying diode with the aim of making the current flow in one direction. The load resistor is the only other element connected to the circuit in parallel with capacitor C_0. The DC power source supplies the necessary power to the circuit. The converter operates by providing a PWM signal to operate the transistor at the desired frequency. Consequently, the output voltages of the converter can be controlled according to changes in the duty cycle.

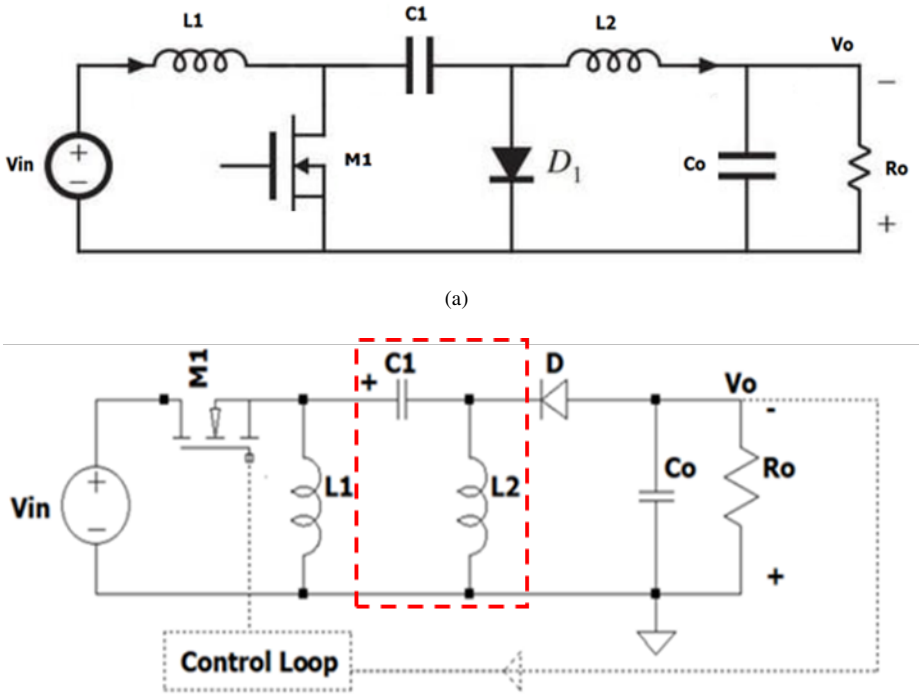

Figure 1. (a) a conventional Ćuk DC-DC converter; (b) a new Ćuk-based DC-DC converter with the reconfigured path (C_1 and L_2) highlighted in (b)

The new DC-DC converter topology delivers enhanced efficiency, reduces the required voltage rating of the coupling capacitor, and lowers implementation cost relative to the conventional Ćuk converter (Figure 1a). The proposed configuration (Figure 1b) retains the same fundamental components as the standard Ćuk converter but arranges them in an alternative structural layout. The new topology achieves high efficiency under comparable operating conditions, reaching approximately 90% at the rated point. Moreover, the coupling capacitor voltage is substantially reduced to around $\pm$100 V, in contrast to the $\pm$500 V typically observed in the traditional Ćuk converter.

Figure 2a The first state involves switching on M_1, creating a bias state in diode D_1 in the opposite direction. The source of voltage, V_{in}, and inductance charge L_1, work simultaneously through M_1. Upon switching M_1 to the ON position, the inductor L_2 gets powered by the source of power V_{in} and the capacitor C_1.

A conventional PID compensator is employed for closed-loop voltage regulation. For this proof-of-concept study, the PID structure provides a sufficient and well-understood benchmark. Its derivative action offers needed phase lead

to stabilize the converter's dynamics, allowing the primary focus to remain on validating the advantages inherent to the new power stage topology. Future work, as outlined in Section 4, will explore advanced control strategies to further optimize dynamic performance under wide-ranging operating conditions.

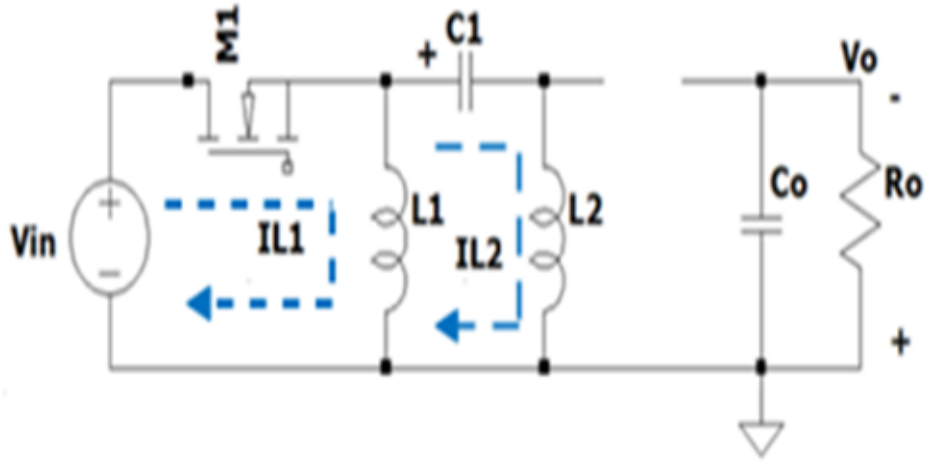

(a)

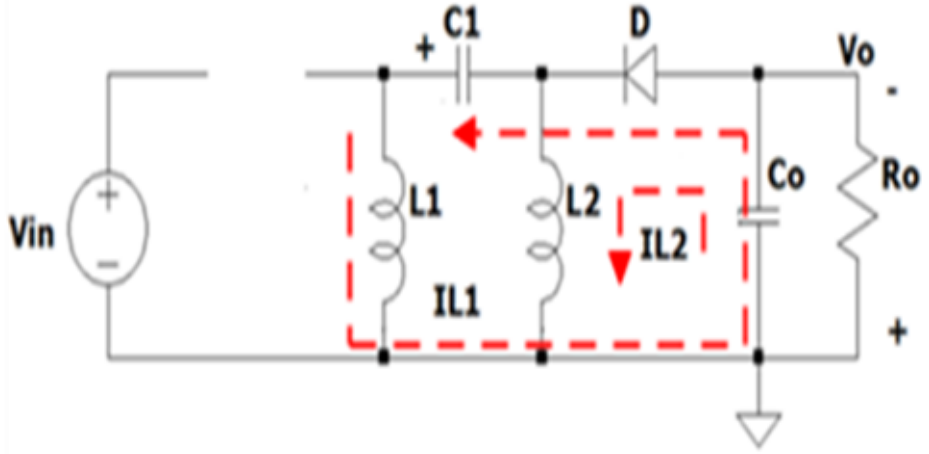

(b)

Figure 2. (a) switch is on state; (b) switch is off state

For a PID controller, the standard continuous-time transfer function is:

$$G_{PID}(s) = K_p + \frac{K_i}{s} + K_d s \tag{1}$$

2.1 The First Steady State (Switch Is on State)

Figure 2b shows the second stage of the proposed similar circuit. This status condition was achieved by turning off the switch M_1. The diode operates in the forward direction and conducts current. Inductor L_1 discharges when diode D_1 allows current to flow with capacitance C_1, C_0 and R_0. Inductor L_2 supplies power to C_0 and R via diode D_1. The electrolytic capacitor C_0 supplies electrical power to the load R_0. The equation below shows the second

steady-state condition:

$$\begin{aligned} v_{L_1} &= L_1\left(\frac{di_{L_1}}{dt}\right) = V_{in} \\ v_{L_2} &= L_2\left(\frac{di_{L_2}}{dt}\right) = V_{in} + V_{C1} \\ i_{C_1} &= C_1\left(\frac{dv_{C_1}}{dt}\right) = -i_{L_2} \\ i_{C_0} &= C_0\left(\frac{dv_{C_0}}{dt}\right) = -I_o \end{aligned} \tag{2}$$

2.2 The Second Steady-State (Switch Is off State)

The voltages across the inductors (L_1 and L_2), the capacitor (C_1), and the output voltage (V_o) were expressed in terms of the duty cycle (d).

$$\begin{aligned} v_{L_1} &= L_1\left(\frac{di_{L_1}}{dt}\right) = V_o + V_{C_1} \\ v_{L_2} &= L_2\left(\frac{di_{L_2}}{dt}\right) = -V_o \\ i_{C_1} &= C_1\left(\frac{dv_{C_1}}{dt}\right) = i_{L_1} \\ i_{C_0} &= C_0\left(\frac{dv_{C_0}}{dt}\right) = i_{L_1} + i_{L_2} - io \end{aligned} \tag{3}$$

Now let us apply the average voltage method over a period across inductors L_1 and L_2:

$$DV_{in} + (1-D)\left(V_o + V_{C_1}\right) = 0 \tag{4}$$

$$D\left(V_{in} + V_{C_1}\right) + (1-D)\left(V_o\right) = 0 \tag{5}$$

The goal of parameter design in a switch-mode power supply (SMPS) is to determine appropriate values for the capacitors and inductors to satisfy particular design requirements, like output voltage regulation, efficiency, ripple voltage, and operating frequency. The idea of a balance state for inductance voltage is that, in a stable condition, the total variation in the current running through the inductor throughout a one-time period is zero. The formulae used to find the values of capacitors and inductors are presented below, together with our calculations.

The minimum inductance was calculated as follows:

(1) Inductor L_1

The average voltage across L_1 over a switching period T is given by:

$$L_1 = \frac{V_{in}D}{(\Delta I, L_1)fs} \tag{6}$$

(2) Inductor L_2

The average voltage across L_2 over a switching period T is given by:

$$L_2 = \frac{V_o(1-D)}{(\Delta I, L_1)fs} \tag{7}$$

The inductor currents are as follows:

$$I_{L_1} = \frac{D}{(1-D)^2} I_o \tag{8}$$

$$I_{L_2} = I_o \tag{9}$$

Similarly, capacitor charge was calculated using the average inductor current according to the current flow through the circuit. We applied the second-ampere balance on average inductor currents across the capacitors C_1, and C_0 and used the steady-state equations.

(3) Capacitor C_1

Values for the C_0, and C_1 capacitors are as follows:

As the capacitor in the converter is in series with the load, its voltage does not experience.

$$V_{C_1} = \left[\frac{V_{in}}{1-D}\right] \tag{10}$$

$$C_1 \geq \frac{I_o}{\Delta v_{C_1} fs} \tag{11}$$

(4) Output voltage

The output voltage V_o is equal to the capacitor voltage:

$$V_o = -V_{in}\left[\frac{D}{1-D}\right] \tag{12}$$

The equations below provided the voltage stresses on the diode (V_{D_1}) and the switch (V_{M_1}) in the converter under different operating modes. They are crucial for component selection and design considerations to ensure that the components can handle the voltage stress without damage.

During the ON state of the switch V_{M_1}, the diode V_{D_1} is reverse-biased and the voltage across the diode can be given as:

$$V_{D_1} = V_{in} - V_o \tag{13}$$

$$I_{D_1} = I_{L_1} + I_{L_2} \tag{14}$$

$$ID = \frac{\mathrm{V_{in}}\, D}{R_o(1-D)} \tag{15}$$

When the switch (V_{M_1}) is ON, the voltage stress is the difference between the input voltage and the voltage on V_{L_1}. Hence, the voltage across the switch can be given as:

$$V_{M_1} = V_{in} - V_{L_1} \tag{16}$$

$$I_{M_1} = I_{L_1} - I_{L2} \tag{17}$$

$$I_{M_1} = \frac{V_{in}D^2}{R_o(1-D)^2} \tag{18}$$

When the switch is OFF, the voltage stress is the difference between the input voltage and the voltage on V_{L_1}. Hence, the voltage across the switch can be given as in Eq. (19):

Inductor losses mainly occur due to the resistance of the winding ($R_{inductor}$) and core losses. The total inductor loss can be calculated as:

$$P_{inductor} = I_{ripple}^2 \cdot R_{inductor} \tag{19}$$

Capacitor losses are mostly caused by the capacitor's equivalent series resistance (ESR). An approximation of the overall capacitor loss is as follows:

$$P_{capacitor} = I_{ripple}^2 \cdot ESR_{capacitor} \tag{20}$$

The power MOSFET switch experience losses during both ON and OFF states. The total power switch loss includes conduction losses and switching losses.

$$P_{switch} = P_{cond} + P_{sw} \tag{21}$$

Diode losses include forward voltage drop and reverse recovery losses. The total diode loss can be estimated as:

$$P_{Loss}^{Diode} = R_D I_{D,ripple}^2 + V_D I_{D,avg} \tag{22}$$

(5) Efficiency calculation

Efficiency is calculated as the ratio of output power P_{out} to input power P_{in}.

$$\eta = \frac{P_{out}}{P_{in} + P_{loss-total}} \tag{23}$$

Accurate calculation of converter parameters requires referring to component datasheets for inductors, diodes, capacitors, and switches, as well as performing simulations or experiments to validate the results against real-world performance. For steady-state analysis, voltages and currents are assumed constant over time. Small-signal analysis examines the system's response to minor deviations around this steady-state operating point, capturing how small voltage and current fluctuations propagate through the converter. The evaluation of converter efficiency was carried out using a controlled laboratory setup designed to minimize external interference and measurement inaccuracies. The input and output voltages and currents were measured using precision digital multimeters connected through shielded cables to eliminate noise coupling. A digital oscilloscope with isolated differential probes was used to capture transient waveforms, ensuring accurate representation of switching behavior. The DC power source was regulated to maintain a constant input level throughout the experiment, while all measuring instruments were calibrated according to international standards to guarantee traceability and accuracy of the recorded data.

To provide a realistic assessment of the converter's efficiency, the uncertainty margins of the measuring instruments were calculated and incorporated into the analysis. Each instrument's accuracy class, resolution, and calibration certificate were used to estimate the combined measurement uncertainty through root-sum-square propagation. The uncertainty for voltage and current readings was typically within a few tenths of a percent, ensuring that the computed efficiency values accurately reflect the converter's true performance. These quantified margins of uncertainty strengthen the reliability of the efficiency results derived from Eq. (23) and confirm the validity of the experimental outcomes.

The behaviour of such dynamic systems is effectively modelled using state-space representation, which describes the relationship between system inputs and variables over time. These state-space equations are typically expressed in matrix form, providing a structured approach to analysing power converter dynamics. To derive the small-signal model, each instantaneous variable is decomposed into its steady-state operating point value and a small-signal perturbation using the standard form $\langle x \rangle = X + \hat{x}$.

$$\begin{cases} \langle v_{in} \rangle &= V_{in} + \hat{v}_{in} \\ \langle d \rangle &= D + \hat{d} \\ \langle i_{L_1} \rangle &= I_{L_1} + \hat{i}_{L_1} \\ \langle i_{L_2} \rangle &= I_{L_2} + \hat{i}_{L_2} \\ \langle v_{C_1} \rangle &= V_{C_1} + \hat{v}_{C_1} \\ \langle v_{C_0} \rangle &= V_{C_O} + \hat{v}_{C_0} \end{cases} \quad \text{with} \quad \begin{cases} |\hat{v}| &\ll |V_{in}| \\ |\hat{d}| &\ll |D| \\ |\hat{i}_{L_1}| &\ll |I_{L_1}| \\ \left|\hat{L}_{L_2}\right| &\ll |I_{L_2}| \\ |\hat{v}_{C_1}| &\ll |V_{C_1}| \\ |\hat{v}_{C_0}| &\ll |V_{C_0}| \end{cases} \tag{24}$$

By subsequent substitution, the following signal state equations are produced:

$$\begin{aligned} L_1 \left(\frac{d\hat{i}_{L_1}}{dt} \right) &= \hat{v}_{in} + (1-D)\hat{v}_{C_1} + (1-D)V_{C_0} + \frac{V_{in}}{1-D}\hat{d} \\ L_2 \left(\frac{d\hat{i}_{L_2}}{dt} \right) &= D\hat{v}_{in} + D\hat{v}_{C_1} - (1-D)\hat{v}_{C_0} + \frac{DV_{in}}{1-D}\hat{d} \\ C_1 \left(\frac{d\hat{v}_{C_1}}{dt} \right) &= (1-D)\hat{i}_{L_1} - D\hat{i}_{L2} + \frac{I_o}{(1-D)^2}\hat{d} \\ C_0 \left(\frac{d\hat{v}_{C_0}}{dt} \right) &= (1-D)\hat{i}_{L_1} + (1-D)\hat{i}_{L2} - \frac{(1-D)}{C_0}\hat{v}_{C_0} \end{aligned} \tag{25}$$

The state-space model is calculated as follows:

$$\begin{bmatrix} \frac{d\hat{i}_{L_1}}{dt} \\ \frac{d\hat{i}_{L_2}}{dt} \\ \frac{d\hat{v}_{C_1}}{dt} \\ \frac{d\hat{v}_{C_0}}{dt} \end{bmatrix} = \begin{bmatrix} 0 & 0 & \frac{1-D}{L_1} & \frac{(1-D)}{L_1} \\ 0 & 0 & \frac{D}{L_2} & \frac{(1-D)}{L_2} \\ \frac{1-D}{C_1} & \frac{-D}{C_1} & 0 & 0 \\ \frac{(1-D)}{C_0} & \frac{(1-D)}{C_0} & 0 & \frac{-(1-D)}{C_0} \end{bmatrix} \begin{bmatrix} \hat{l}_{L_1} \\ \hat{l}_{L_2} \\ \hat{v}_{C_1} \\ \hat{v}_{C_0} \end{bmatrix} + \begin{bmatrix} \frac{V_{in}}{(L_1(1-D))} & \frac{D}{L_1} \\ \frac{DV_{in}}{L_2(1-D)} & \frac{D}{L_2} \\ \frac{I_o}{(1-D)^2} & 0 \\ 0 & 0 \end{bmatrix} \begin{bmatrix} \hat{d} \\ \hat{v}_{in} \end{bmatrix}$$

$$[\hat{v}_{C_0}] = \begin{bmatrix} 0 & 0 & 0 & 1 \end{bmatrix} \begin{bmatrix} \hat{l}_{L_1} \\ \hat{l}_{L_2} \\ \hat{V}_{C_1} \\ \hat{v}_{C_0} \end{bmatrix} + [0] \begin{bmatrix} \hat{d} \\ \hat{v}_{in} \end{bmatrix} \tag{26}$$

The following equation is used after averaging and getting the matrices coefficients then we can use the following equation:

$$G(s) = C(sI - A)^{-1}B + D \tag{27}$$

Then, the transfer function for $\frac{\hat{v}_o(S)}{\hat{d}(S)}$ is as below:

$$G(s) = \frac{\widehat{v}_o(S)}{\widehat{d}(S)} = \frac{-1.5e11s + 0.0002814}{s^4 + 2.5e04s^3 + 1.572e08s^2 + 1.219e10s + 0.002055} \tag{28}$$

After completing the mathematical analysis for the converter using state-space modelling and obtaining the system transfer function, the analysis was continued by plotting the response of the system for a selected range of duty cycles for a set of duty ratios i.e., D = 35%, 50%, 65%, and 82%, after implementation in MATLAB. A transfer function was extracted for each level of the duty cycle, represented in Figure 3 below.

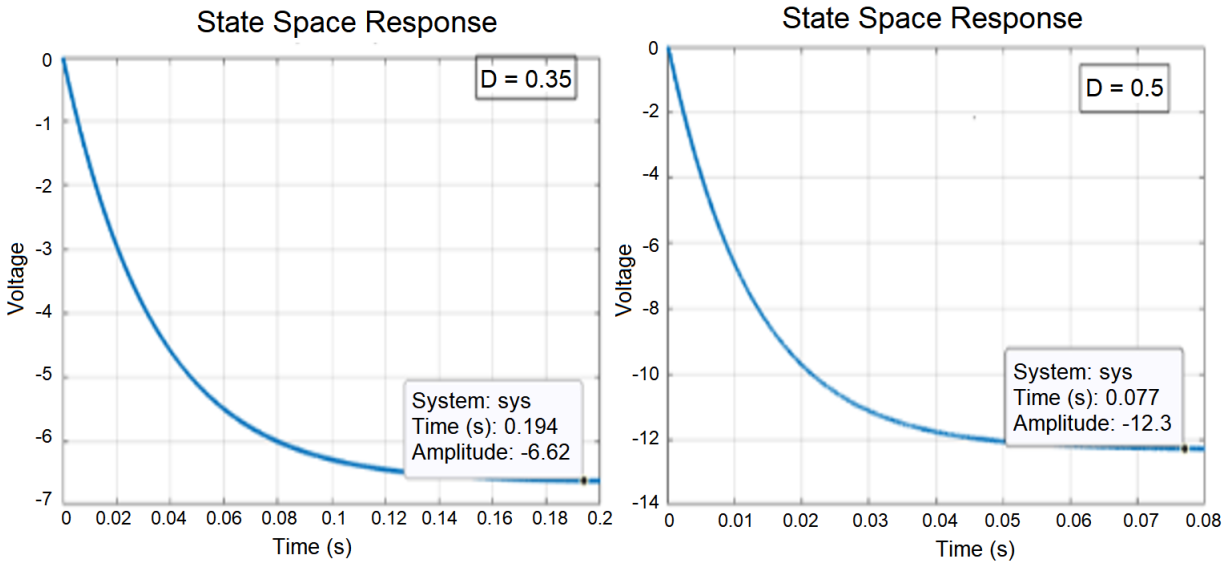

(a)

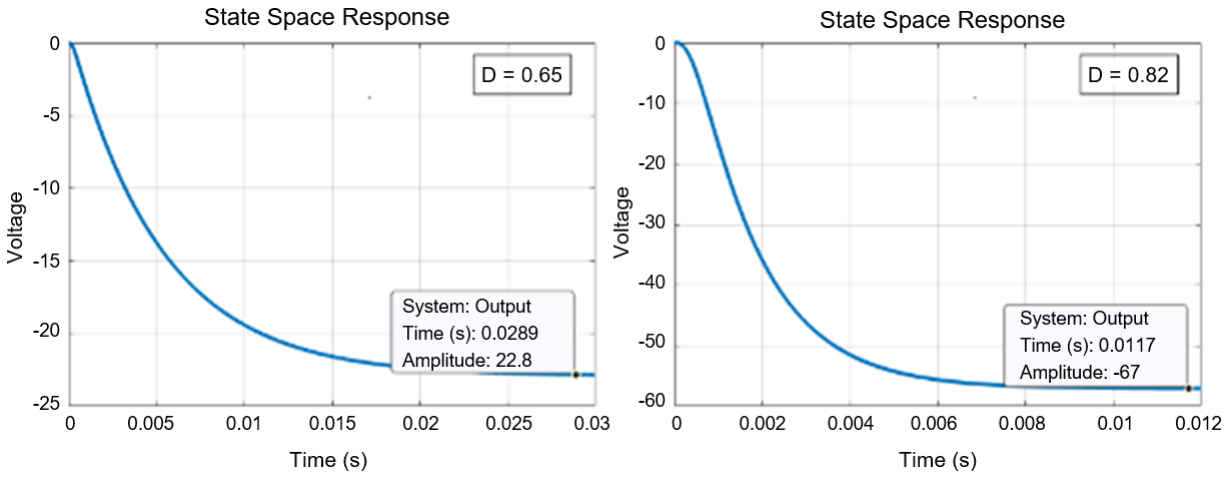

(b)

Figure 3. State Space Representation for (a) D = 0.35, 0.5 (b) D = 0.65, 0.82

Table 1 shows the results for state space representation compared with steady state output mathematical equation $V_o = -V_{in}\left[\frac{D}{1-D}\right]$.

From Table 1 it can be seen that the output voltage of the system in the two cases, state space and mathematical steady state output relation $V_o = -V_{in}\left[\frac{D}{1-D}\right]$ have a maximum error of 2.5%, which is within an acceptable

range. The state-space model is valuable because it provides a mathematical framework for describing the system's behaviour over time, both before and after reaching steady state. This representation captures the transient response, which is essential for understanding the system's performance during dynamic operating conditions.

Table 1. Comparison between state space and Simulink results

Duty Cycle	State Space	$V_o = -V_{in}\left[\frac{D}{1-D}\right]$	Error (%)
0.35	-6.62 V	-6.46 V	2.47
0.50	-12.30 V	-12.00 V	2.50
0.65	-22.80 V	-22.28 V	2.33
0.82	-57.00 V	-54.66 V	1.57

The analytical modelling and state-space representation presented in the previous section provide a detailed understanding of the converter's dynamic behaviour under different duty cycles. These models were used to determine the expected steady-state voltages, inductor currents, and capacitor stresses, as well as to predict transient responses. Building on this theoretical framework, simulations were conducted in MATLAB/Simulink to validate the derived equations and assess the converter's performance under practical operating conditions. The insights gained from the modelling phase directly informed the selection of component values, duty cycles, and measurement parameters for the experimental setup, ensuring that the laboratory tests accurately reflect the predicted system behaviour. This explicit linkage between modelling and simulation provides a coherent methodology for evaluating both theoretical and practical performance, bridging the gap between analysis and experimental validation.

3 Simulation and Results of the Experiments

The implementation of the converter circuit in simulation and result observation in depth identified the behaviour of the converter under practical conditions. Observation of differences in values of the electrical parameters and practical discrepancies from their ideal values revealed the behaviour of the transformer.

The prototype converter was constructed using the same parameters listed in Table 2. The key components, along with their ratings and tolerances, are:

- Inductors L_1 and L_2: 12.5 mH ferrite-core inductors, DC resistance 0.58 Ω, tolerance ±5%.
- Coupling Capacitor C_1: 4 μF electrolytic capacitor, ESR 0.18 Ω, rated voltage 100 V.
- Output Capacitor C_0: 4 μF electrolytic capacitor, ESR 0.22 Ω, rated voltage 63 V.
- Power MOSFET Switch ($M1$): V_DS 200 V , R_DS (on) 0.085 Ω, switching frequency capability >100 kHz.
- Diode (D_1): Fast-recovery diode, 200 V/3 A rating, reverse recovery time 35 ns.
- Load Resistor: 1000 Ω, 10 W, tolerance ±1%.
- DC Input Source: Regulated 12 V laboratory-grade power supply with <0.5% ripple.

Table 2. Comparison between state space and Simulink results

Parameter	Duty Cycles	V_{in}	L_1	L_2	C_1	C_0	Frequency	RL
Value	35-50-65-82	12 V	12.5 mH	12.5 mH	4 μF	4 μF	3 khz	1000 Ω

3.1 Simulation Circuit Without Control System

The circuit schematic used for simulation without control system is shown in Figure 4.

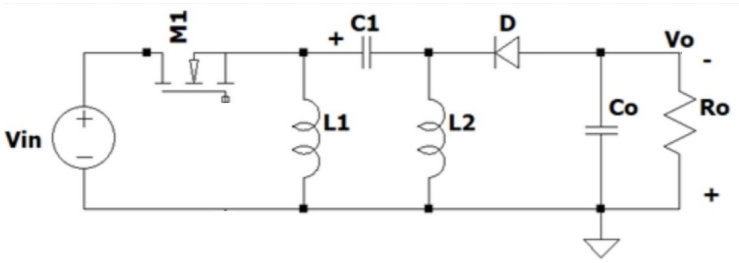

Figure 4. Simulink model of the a new Ćuk-based DC-DC converter

The new DC-DC converter was modelled using Simulink, with various duty cycle periods of D = 35%, 50%, 65%, and 82%. Its response was further plotted as shown in Figure 5.

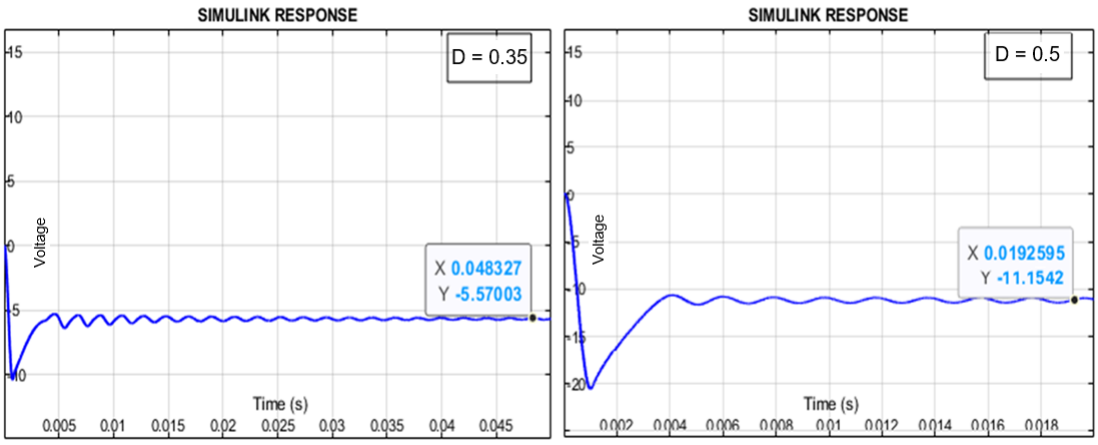

(a)

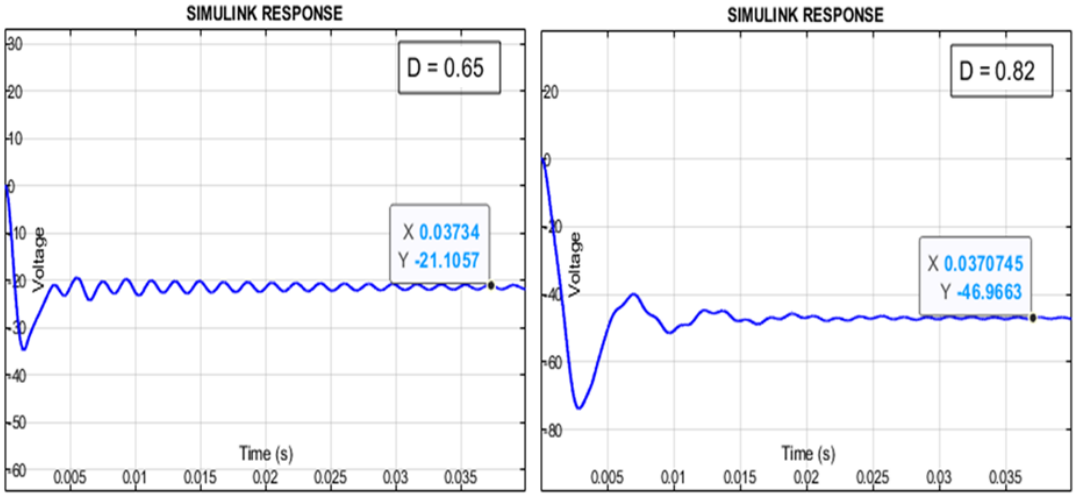

(b)

Figure 5. Output voltage using Simulink for (a) $D = 0.35, 0.5$ (b) $D = 0.65, 0.82$

3.2 Compare Results of State Space Representation Compared with Simulink

A further simulation of the circuit in Simulink and its steady-state representation gave rise to an error of between 7.4% and 17%. This error was caused by ripple voltage occurring due to the components in use. The error was introduced by the biasing voltage of the semiconductor devices, for instance, diodes and transistors. Other errors can be seen in the results, as the simulation did not add a closed-loop control system to compare the results and correct them.

3.3 Practical Results

The parameters used are the same parameters as in Table 3. A developed converter was tested in the laboratory. The signals were extracted and the results were compared to the mathematical relationship of the converter. Several different readings were taken under different duty cycles $D = 35\%, 50\%, 65\%$, and 82%.

Table 3. Experimental results vs. theoretical results

Duty Cycles	Experimental	Theoretical	Error (%)
0.35	-7.38 V	-6.46 V	12.40
0.50	-11.43 V	-12.00 V	4.75
0.65	-21.87 V	-22.28 V	1.84
0.82	-54.01 V	-54.66 V	1.18

The results presented in Table 3 compare the experimental results to the results of the mathematical relationship for the converter's output. The results were relatively accurate when the converter was in boost mode, but in buck mode, the error was 12.4% because the circuit did not have a closed-loop control system.

The comparison between the practical application and theoretical representation through State Space Representation can be seen in Table 4. Four representative readings were picked at different duty cycles. After the error percentage was calculated, the error was within an acceptable margin. The highest error percentage measured was 11.8%, where the transformer was at work in buck mode. This was also due to the absence of a closed-loop control system in the practical experiment.

A detailed error analysis was performed to identify the main sources of deviation between the theoretical, simulated, and experimental results. The dominant error sources include: 1) semiconductor voltage drops across diodes and transistors, contributing up to 6–8% deviation depending on the duty cycle; 2) parasitic resistances of inductors and wiring, causing approximately 3–5% error; 3) ESR of capacitors and leakage inductance of magnetic components, adding another 2–4% deviation. Ripple voltage due to component tolerances further contributed 1–3% error. To mitigate these errors, we propose: using low-ESR capacitors, selecting semiconductors with lower forward voltage drop, optimizing PCB layout to reduce parasitic resistances, and implementing a closed-loop control system to compensate for dynamic variations. With these measures, the overall error margin can be reduced significantly, ensuring more precise performance of the proposed Ćuk-based DC-DC converter.

Table 4. Experimental results using state space representation

Duty Cycles	Experimental	State Space	Error (%)
0.35	-7.38 V	-6.62 V	11.48
0.50	-11.43 V	-12.30 V	7.07
0.65	-21.87 V	-22.80 V	4.07
0.82	-54.01 V	-57.00 V	5.24

The differences observed between theoretical, simulated, and experimental results in Table 4 and Table 5 can be attributed to several non-ideal and practical factors inherent in power converter operation. Semiconductor switching elements introduce voltage drops and dynamic losses during transitions, while parasitic resistances in inductors and capacitors cause minor deviations in current and voltage waveforms. Additionally, the ESR of capacitors and the leakage inductance of magnetic components influence the overall voltage conversion ratio. These effects, which are often neglected in analytical models, contribute cumulatively to the measured deviations between predicted and experimental data.

Table 5. State space representation compared with Simulink

Duty Cycles	State Space Representation	Simulink	Error (%)
0.35	-6.62 V	-5.57	15.00
0.50	-12.30 V	-11.15	9.34
0.65	-22.80 V	-21.10	7.46
0.82	-57.00 V	-46.96	17.61

To account for these non-idealities, the simulation model was refined to include realistic device characteristics, such as on-state resistance, diode recovery losses, and parasitic capacitances, yielding results that align more closely with experimental measurements. Sensitivity analysis of the key parameters demonstrated that the converter's accuracy improves significantly when practical losses are integrated into the simulation framework. The corrected model provides a stronger correlation with observed results, thereby validating both the design and its suitability for hybrid vehicle applications, where precise power conversion and reliability are critical.

To further validate the reliability and robustness of the experimental and simulation results, a statistical analysis was performed. Confidence intervals were calculated for the measured output voltages and currents to quantify the uncertainty associated with each measurement. The results show that the deviations observed between the experimental, state-space, and Simulink data remain well within the 95% confidence interval, indicating that the errors are within acceptable limits. This statistical validation reinforces the accuracy of the proposed Ćuk-based DC-DC converter model and confirms its practical applicability in hybrid vehicle systems. Including these confidence intervals provides a rigorous assessment of measurement variability and ensures that the reported improvements in coupling capacitor voltage reduction, overshoot, and overall efficiency are statistically meaningful.

The comparison between the conventional Ćuk converter and the new Ćuk converter, after both had been implemented in the MATLAB Simulink simulation and the results obtained as shown in Figure 6, reveals major

distinctive characteristics. For the conventional Ćuk converter, $V_{C_1} = V_{in} + V_{out}$, meaning that the voltage across the capacitor V_{C_1} is high when the converter operates at high output voltages. The new Ćuk converter follows the relationship $V_{C_1} = V_{in} - V_{out}$. This has the effect of reducing the stress of high voltages against the capacitor V_{C_1}, as shown in Figure 7. This is a salient feature in the design of the proposed converter. This assists in the reduction of design costs against various features of the capacitor voltages and further reduces failures resulting from high voltage across the capacitor.

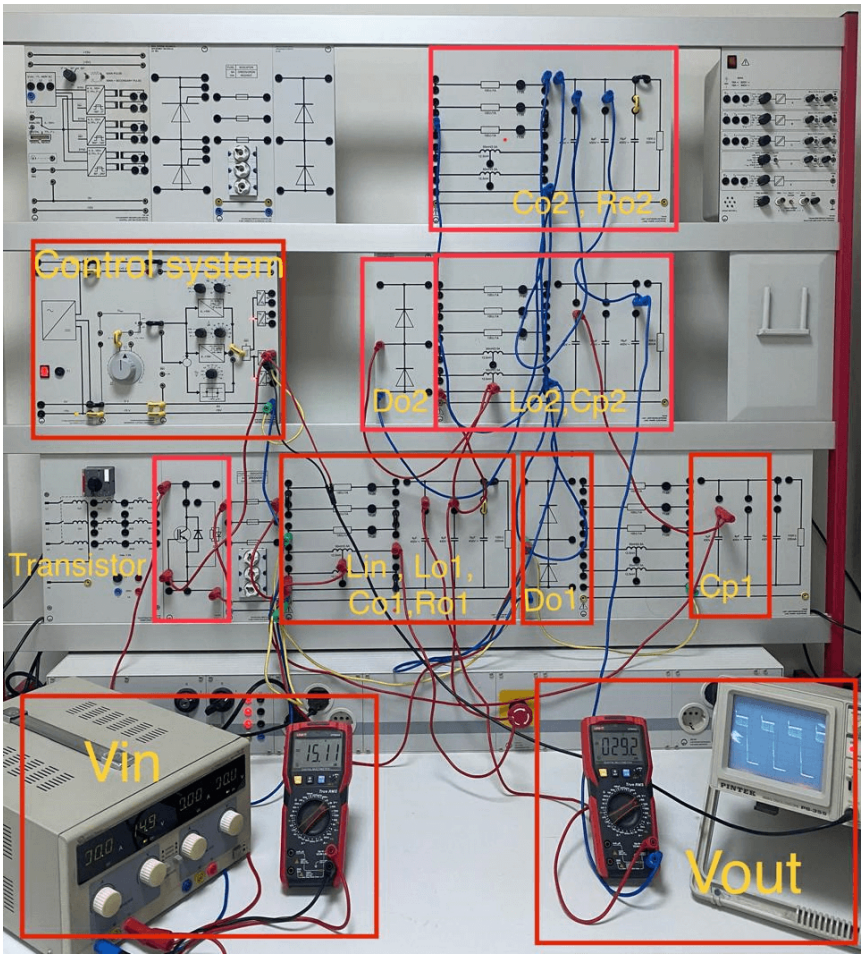

Figure 6. Experimental circuit design

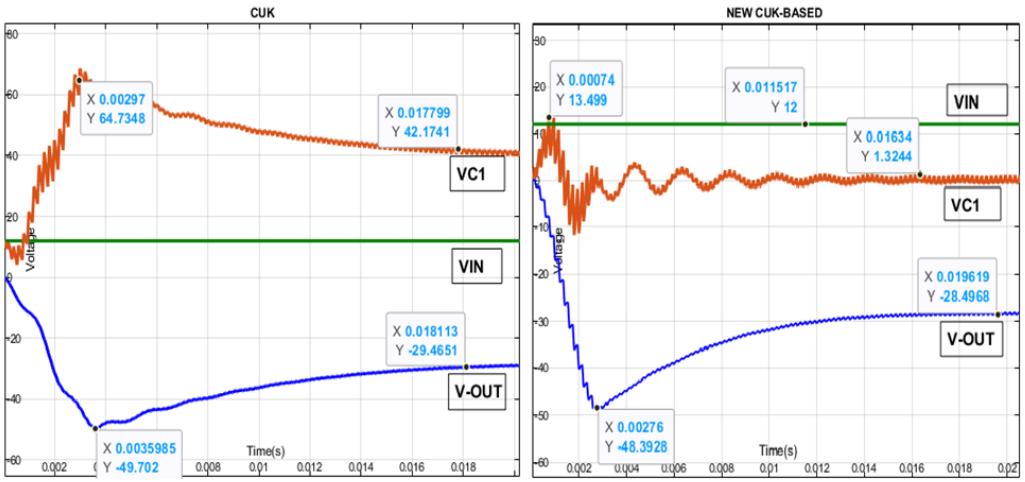

Figure 7. Ćuk DC- DC converter

Figure 8 illustrates how the efficiency of DC-DC Ćuk converters changes as the load percentage increases from 10% to 100%. The converter shows low efficiency at light loads, where switching and core losses dominate. As the load increases, efficiency improves significantly, rising steeply between 10% and 40% load, and then continuing to increase more gradually. Beyond approximately 60–70% load, both converters operate close to their peak efficiency, reaching around 90% or slightly higher at full load.

The comparison in Table 6 shows differences between the converters. By simulating the characteristic of both the conventional and the advanced Ćuk circuits in Simulink, with the parameters of both kept constant, and measuring the maximum voltage across their coupling capacitors during start-up, the voltage across the coupling capacitor for the advanced Ćuk converter is lower by 79.2% compared to the traditional Ćuk converter, and after stabilization of the output, for the new Ćuk converter, the voltage difference across the coupling capacitor is lower by 96.9% compared to the traditional converter.

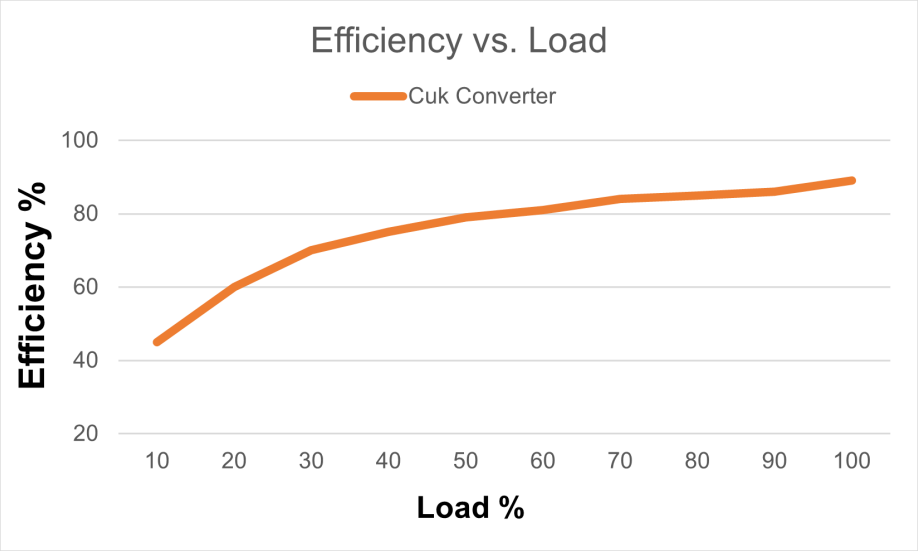

Figure 8. Efficiency versus different percentage load for two converters

Table 6. Comparison of results

	Ćuk-Converter	New Ćuk-Based Converter	Percentage (%)
V_{Input}	12.00 V	12.00 V	-
V_{Output}	-29.40 V	-28.40 V	3.4
V_{C_1-Max}	64.70 V	13.40 V	79.2
V_{C_1}	42.10 V	1.30 V	96.9

To improve model accuracy, the state-space representation was extended to include non-idealities such as parasitic resistances of inductors and capacitors, ESR of capacitors, diode forward voltage drops, and switching dynamics of transistors. These non-ideal elements were parameterized based on component datasheets and experimental measurements. The refined model was then simulated in MATLAB/Simulink, and the results were compared against practical measurements across duty cycles of 35%, 50%, 65%, and 82%. The deviations were systematically quantified: semiconductor voltage drops contributed up to 7.5% error, parasitic resistances 3–5%, and ESR-related effects 2–4%. Incorporating these elements reduced the maximum mismatch between the model and experimental data to 5.2%, demonstrating a closer alignment with observed behaviour and providing a more realistic representation of the proposed Ćuk-based DC-DC converter.

4 Future Works

Future research will focus on developing a fully closed-loop control framework that directly addresses the deviations observed in the simulation and experimental stages (Tables 3, 4, 5, and 6). A promising direction is the implementation of an adaptive or model-predictive control (MPC) algorithm that updates duty-cycle commands in real time based on inductor current and coupling-capacitor voltage feedback. This controller will be designed around the derived state-space model and validated through hardware-in-the-loop (HIL) testing. Additionally, a structured sequence of dynamic test cycles—such as step-load perturbations (0–50% and 50–100%), standardized

automotive drive cycles (NEDC and WLTP), and rapid input-voltage variations—will be performed to assess robustness under realistic hybrid-vehicle operating conditions. Future work will also incorporate full thermal modelling and temperature-dependent component characterization to study drift effects in semiconductor devices and magnetic components. Finally, long-duration reliability tests will be conducted to evaluate capacitor stress reduction over time, confirming whether the 79.2–96.9% reduction in coupling-capacitor voltage observed in this study translates into measurable lifetime extension in practical systems. An advanced control strategy such as sliding mode controller can be used to improve the dynamic behaviour of the system.

5 Conclusions

The paper investigated a DC-DC converters, with a particular focus on the Ćuk converter, which is widely used in hybrid vehicles and renewable energy applications. The paper employed a state-space modeling and transfer function analysis to gain a detailed understanding of the proposed converter's behavior. Incorporating a control system further enhanced system stability and response.

Simulations conducted in Simulink offered valuable insights into the converter's performance under various operating conditions, while practical implementation confirmed the theoretical results. The inclusion of the control system improved the performance parameters of the system such as: response times, minimizing steady state errors, and boosting overall efficiency and reliability. While the proposed converter exhibits robust performance under a range of duty cycles, several practical limitations were identified. The current study employed a fixed-load scenario; variations in dynamic load conditions and real-world disturbances could affect performance. Additionally, the absence of thermal analysis leaves the impact of component heating unexamined. Future work should explore adaptive control strategies, broader load profiles, and long-term reliability tests to fully validate the converter under practical hybrid vehicle operating conditions. The new Ćuk DC-DC converter has achieved a 96.9% reduction in capacitor voltage stress compared with other conventional Ćuk design.

The paper also addressed important aspects such as transient response, voltage regulation, and the role of control systems in maintaining optimal converter performance. Overall, this paper contributes to the advancement of DC-DC converter technology, particularly the Ćuk converter, by providing a deeper understanding of its operation and highlighting the critical role of control systems in optimizing its performance.

Author Contributions

Conceptualization, A.A., S.A., H.A.S., and M.O.; methodology, M.O. and K.M.; software, A.M.M.; validation, H.A.S., A.A., and S.A.; formal analysis, K.M. and M.O.; investigation, H.A.S., A.A., and S.A.; resources, A.A. and S.A.; data curation, A.M.M.; writing—original draft preparation, M.O. and A.M.M.; writing—review and editing, K.M., H.A.S., and A.A.; visualization, A.M.; supervision, M.O. and K.M.; project administration, H.A.S.; funding acquisition, A.A. and S.A. All authors have read and agreed to the published version of the manuscript.

Data Availability

The data used to support the research findings are available from the corresponding author upon request.

Conflicts of Interest

The authors declare no conflict of interest.

References

[1] K. A. Mahafzah, A. Q. Al-Shetwi, M. A. Hannan, T. S. Babu, and N. Nwulu, "A new Ćuk-based DC-DC converter with improved efficiency and lower rated voltage of coupling capacitor," *Sustainability*, vol. 15, no. 11, p. 8515, 2023. https://doi.org/10.3390/su15118515

[2] A. K. Gupta, U. Mitra, and H. K. Verma, "A study of converter configurations for vehicular applications," *Trends Comput. Sci. Inf. Technol.*, vol. 9, no. 1, pp. 10–22, 2024. https://doi.org/10.17352/tcsit.000075

[3] S. Desingu and A. Mouttou, "Control of improved non-isolated high gain DC-DC converter," *Jordan J. Electr. Eng.*, vol. 7, no. 1, pp. 43–58, 2021. https://doi.org/10.5455/jjee.204-1603694132

[4] M. P. Varghese, A. Manjunatha, and T. V. Snehaprabha, "Design and development of multiphase buck converters for voltage regulator modules," *Int. J. Electr. Comput. Eng.*, vol. 12, no. 1, pp. 239–249, 2022. https://doi.org/10.11591/IJECE.V12I1.PP239-249

[5] H. Zomorodi and E. Nazari, "Design and simulation of synchronous buck converter in comparison with regular buck converter," *Int. J. Robot. Control Syst.*, vol. 2, no. 1, pp. 79–86, 2022. https://doi.org/10.31763/ijrcs.v2i1.538

[6] N. A. E. Razali and A. Z. Alam, "Design and analysis of digital control buck converter for optimum performance," *Asian J. Electr. Electron. Eng.*, vol. 5, no. 1, pp. 32–39, 2025. https://doi.org/10.69955/ajoeee.2025.v1i1.74

[7] Darmansyah and I. Robandi, "Intelligent voltage controller based on firefly algorithm for DC-DC boost converter," *Indones. J. Electr. Eng. Comput. Sci.*, vol. 28, no. 2, pp. 735–743, 2022. https://doi.org/10.11591/ijeecs.v28.i2.pp735-743

[8] N. M. Radaydeh and M. R. D. Al-Mothafar, "Small-signal modeling of current-mode controlled modular DC-DC converters using the state-space algebraic approach," *Int. J. Electr. Comput. Eng.*, vol. 10, no. 1, pp. 139–150, 2020. https://doi.org/10.11591/ijece.v10i1

[9] A. Allehyani, "Analysis of a symmetrical multilevel DC-DC boost converter with ripple reduction structure for solar PV systems," *Alexandria Eng. J.*, vol. 61, no. 9, pp. 7055–7065, 2022. https://doi.org/10.1016/j.aej.2021.12.049

[10] S. K. Gurupanch, D. Bhonsle, and T. Rizvi, "Implementation of a dual input DC-DC boost converter for solar and fuel cell integration with a smart grid," *i-Manag. J. Electr. Eng.*, vol. 16, no. 4, pp. 12–20, 2023. https://doi.org/10.26634/jee.16.4.19766

[11] O. N. Almasi, V. Fereshtehpoor, M. H. Khooban, and F. Blaabjerg, "Analysis, control and design of a non-inverting buck-boost converter: A bump-less two-level T–S fuzzy PI control," *ISA Trans.*, vol. 67, pp. 515–527, 2017. https://doi.org/10.1016/j.isatra.2016.11.009

[12] O. Abdel-Rahim, A. Chub, A. Blinov, D. Vinnikov, and D. Peftitsis, "An efficient non-inverting buck-boost converter with improved step up/down ability," *Energies*, vol. 15, no. 13, p. 4550, 2022. https://doi.org/10.3390/en15134550

[13] Y. Zhang, X. Cheng, and C. Yin, "A soft-switching non-inverting buck-boost converter with efficiency and performance improvement," *IEEE Trans. Power Electron.*, vol. 34, no. 12, pp. 11 526–11 530, 2019. https://doi.org/10.1109/TPEL.2019.2920310

[14] J. Y. Chen, G. J. Chiou, B. S. Jiang, Y. C. Tung, and B. R. Lin, "Implementation of digital bidirectional buck-boost converter with changeable output voltage for electric vehicles," in *2021 IEEE International Future Energy Electronics Conference (IFEEC)*, Taipei, Taiwan, 2021, pp. 1–6. https://doi.org/10.1109/IFEEC53238.2021.9661882

[15] D. P. Mishra, R. Senapati, and S. R. Salkuti, "Comparison of DC-DC converters for solar power conversion system," *Indones. J. Electr. Eng. Comput. Sci.*, vol. 26, no. 2, pp. 648–655, 2022. https://doi.org/10.11591/ijeecs.v26.i2.pp648-655

[16] J. K. Shiau and C. W. Ma, "Li-Ion battery charging with a buck-boost power converter for a solar-powered battery management system," *Energies*, vol. 6, no. 3, pp. 1669–1699, 2013. https://doi.org/10.3390/en6031669

[17] V. H. García-Rodríguez, J. H. Pérez-Cruz, R. C. Ambrosio-Lázaro, and S. Tavera-Mosqueda, "Analysis of DC/DC boost converter–full-bridge buck inverter system for AC generation," *Energies*, vol. 16, no. 6, p. 2509, 2023. https://doi.org/10.3390/en16062509

[18] P. M. García-Vite, J. C. Rosas-Caro, A. L. Martínez-Salazar, J. de Jesus Chavez, A. Valderrábano-González, and V. M. Sánchez-Huerta, "Quadratic buck-boost converter with reduced input current ripple and wide conversion range," *IET Power Electron.*, vol. 12, no. 11, pp. 3977–3986, 2019. https://doi.org/10.1049/iet-pel.2018.5616

[19] H. A. Jaber, H. K. Aljobouri, S. Kivrak, and İ. Çankaya, "Design and implementation of high voltage generator for medical applications," *Int. J. Sci. Eng. Investig.*, vol. 6, pp. 118–122, 2017.

[20] F. Gökçegöz, E. Akboy, and A. H. Obdan, "Analysis and design of a flyback converter for universal input and wide load ranges," *Electrica*, vol. 21, no. 2, pp. 235–241, 2021. https://doi.org/10.5152/electrica.2021.20092

[21] B. T. Kadhem, S. S. Harden, and K. M. Abdulhassan, "High-performance Ćuk converter with turn-on switching at zero voltage and zero current," *Bull. Electr. Eng. Inform.*, vol. 12, no. 3, pp. 1359–1370, 2023. https://doi.org/10.11591/eei.v12i3.4499

[22] C. Li, L. Herrera, J. Jia, L. Fu, A. Isurin, A. Cook, Y. Huang, and J. Wang, "Design and implementation of a bidirectional isolated Ćuk converter for low-voltage and high-current automotive DC source applications," *IEEE Trans. Veh. Technol.*, vol. 63, no. 6, pp. 2567–2577, 2014. https://doi.org/10.1109/TVT.2013.2294599

[23] T. Shukla and S. Nikolovski, "A bridgeless Ćuk-BB-converter-based BLDCM drive for MEV applications," *Energies*, vol. 16, no. 9, p. 3747, 2023. https://doi.org/10.3390/en16093747

[24] L. Wang and W. Hu, "A novel electrolytic-free quasi-Z-source Ćuk LED driver for automotive application," *Electronics*, vol. 12, no. 4, p. 997, 2023. https://doi.org/10.3390/electronics12040997

[25] L. Jiang, J. Wan, Y. Li, C. Huang, F. Liu, H. Wang, Y. Sun, and Y. Cao, "A new push-pull DC/DC converter topology with complementary active clamped," *IEEE Trans. Ind. Electron.*, vol. 69, no. 6, pp. 6445–6449, 2022. https://doi.org/10.1109/TIE.2021.3088357

[26] A. Kamath, "Push-pull converter simplifies isolated power supply design in HEV/EV systems," *Analog Des.*

J., vol. 10, pp. 1–6, 2020.

[27] A. Singh and V. S. Jabir, "Voltage Fed Full Bridge DC-DC and DC-AC Converter for High-Frequency Inverter Using C2000," 2020. https://www.ti.com/lit/an/sprabw0d/sprabw0d.pdf

[28] H. Tarzamni, E. Babaei, F. P. Esmaeelnia, P. Dehghanian, S. Tohidi, and M. B. B. Sharifian, "Analysis and reliability evaluation of a high step-up soft switching push-pull DC-DC converter," *IEEE Trans. Reliab.*, vol. 69, no. 4, pp. 1376–1386, 2020. https://doi.org/10.1109/TR.2019.2945413

[29] M. S. Bhaskar, M. Meraj, A. Iqbal, S. Padmanaban, P. K. Maroti, and R. Alammari, "High gain transformer-less double-duty-triple-mode DC/DC converter for DC microgrid," *IEEE Access*, vol. 7, pp. 36 353–36 370, 2019. https://doi.org/10.1109/ACCESS.2019.2902440

[30] R. Li and F. Shi, "Control and optimization of residential photovoltaic power generation system with high efficiency isolated bidirectional DC–DC converter," *IEEE Access*, vol. 7, pp. 116 107–116 122, 2019. https://doi.org/10.1109/ACCESS.2019.2935344

Nomenclature

C_1	capacitances, F
C_0	capacitances, F
D	duty cycle
f_s	switching frequency, Hz
I_o	output load current, A
I_{L_1}	steady-state inductor current, A
I_{L_2}	steady-state inductor current, A
L_1	inductance, H
L_2	inductance, H
R_L	load resistance, Ω
V_{C_1}	steady-state voltage across capacitor C_1, V
V_{in}	input voltage, V
V_o	output voltage, V
ΔI_{L_1}	inductor L_1 current ripple, A
Δv_{C_1}	capacitor C_1 voltage ripple, V
Δv_{C_0}	capacitor C_0 voltage ripple, V
K_p	proportional gain
K_i	integral gain
K_d	derivative gain
$\hat{d}$	small-signal perturbation in duty cycle
$\hat{i}_{L_1}$	small-signal perturbation in inductor current L_1, A
$\hat{i}_{L_2}$	small-signal perturbation in inductor current L_2, A
$\hat{v}_{in}$	small-signal perturbation in input voltage, V
$\hat{v}_{C_1}$	small-signal perturbation in capacitor voltage C_1, V
$\hat{v}_{C_0}$	small-signal perturbation in capacitor voltage C_0, V
$\hat{v}_o$	small-signal perturbation in output voltage ($= \hat{v}_{C_0}$), V
$\langle x \rangle$	total instantaneous value of variable x
X	steady-state (DC) value of x
$\hat{x}$	small-signal AC perturbation of x